

Liang, L. et al. (2018) Unity integration of grating slot waveguide and microfluid for terahertz sensing. *Laser and Photonics Reviews*, 12(11), 1800078.

There may be differences between this version and the published version. You are advised to consult the publisher's version if you wish to cite from it.

Liang, L. et al. (2018) Unity integration of grating slot waveguide and microfluid for terahertz sensing. *Laser and Photonics Reviews*, 12(11), 1800078. (doi:[10.1002/lpor.201800078](https://doi.org/10.1002/lpor.201800078))

This article may be used for non-commercial purposes in accordance with [Wiley Terms and Conditions for Self-Archiving](#).

<http://eprints.gla.ac.uk/171410/>

Deposited on: 06 November 2018

Unity Integration of Grating Slot Waveguide and Microfluid for Terahertz Sensing

Li Liang^{1,2,3,#}, Xin Hu^{2,#}, Long Wen^{1,}, Yuhuan Zhu², Xianguang Yang¹, Jun Zhou⁴, Yaxin Zhang⁴, Ivonne Escorcia Carranza⁵, James Grant⁵, Chunping Jiang², David R. S. Cumming^{5,*}, Baojun Li¹, Qin Chen^{1,*}*

*Corresponding Author: E-mail: longwen@jnu.edu.cn; David.Cumming.2@glasgow.ac.uk; chenqin2018@jnu.edu.cn

¹ Guangdong Provincial Key Laboratory of Optical Fiber Sensing and Communications, Institute of Nanophotonics, Jinan University, Guangzhou 511443, P. R. China

² Key Lab of Nanodevices and Applications-CAS, Suzhou Institute of Nano-Tech and Nano-Bionics, Chinese Academy of Sciences (CAS), Suzhou 215123, P. R. China.

³ School of Nano Technology and Nano Bionics, University of Science and Technology of China, Hefei 230026, P. R. China

⁴ Terahertz Science Cooperative Innovation Center, University of Electronic Science and Technology of China, Chengdu 610054, P.R. China

⁵ School of Engineering, University of Glasgow, Glasgow G12 8LT, UK

equal contribution

Abstract

Refractive index sensing is attracting extensive interest. Limited by the weak light-matter interaction and the broad bandwidth of resonance, the figure of merit (FoM) of terahertz (THz) sensors is much lower than their counterparts in visible and infrared regions. Here, these two issues are addressed by incorporating a microfluidic channel as a slot layer into a grating slot waveguide (GSW), where guided-mode resonance results in a narrowband resonant peak and the sensitivity increases remarkably due to the greatly concentrated electromagnetic fields in the slot layer. Both reflective and transmissive sensors are developed with the calculated quality (Q) factors two orders of magnitude larger than metamaterial and plasmonic sensors, and the sensitivities one order of magnitude larger than grating waveguide sensors, contributing to a record high FoM of 692. The measured results match well with the simulations considering the fabrication errors, where the degeneration of narrowband transmission peaks in experiments is attributed to the error of the microfluidic channel height and the divergence of the incident beam. The proposed unity-integrating configuration with

simultaneous optimizations of the resonance mechanism, and the spatial overlap between the sensing field and the analytes shows the potential for high sensitivity bio and chemo sensing.

1. Introduction

Terahertz (THz) waves provide unique fingerprints of bio and chemo species caused by the rotational and vibrational modes of molecules.^[1, 2] This characteristic of the electromagnetic region provides promising applications in the area of bio-chemical research, especially label-free detection of refractive index change induced by molecular interactions.^[3] To improve the light-matter interaction between the long-wavelength THz wave and the analytes, various micro-/nanostructures with strong confinements have been utilized for sensor design, such as resonators,^[4] photonic crystals (PC),^[5] nanowires,^[6] plasmonic structures,^[7,8] and metamaterials.^[9, 10] In most cases, the evanescent fields of the resonant modes are applied for sensing. It is crucial to place the analytes where the concentration of electric-field is the largest. Recently, some of the authors have demonstrated a remarkable increase of the sensitivity (S) via the localized resonant field sensing by integrating the microfluidic channel between metal reflector and metal microstructures to form a THz metamaterial absorber (MA), which has strongly confined electromagnetic fields between two metal layers.^[11] This unity-integrating configuration provides greatly increased spatial overlap between the localized field and the analytes. Similar improvements have also been observed by partially etching away the intermediate layer of MA.^[12] However, for a resonant optical biosensor based on the detection of the refractive index change, a figure of merit (FoM) defined by the ratio of the sensitivity to the linewidth of the resonance is usually used to evaluate the actual device performance.^[13] Therefore, a large sensitivity does not ensure a low detectivity if the resonant peak is too broad. For example, the low quality (Q) factors (<10) of the above mentioned MA sensors finally limit the FoMs (<10). A narrow linewidth, that is, a high Q

factor, has a positive effect in the light-matter interaction and contributes to the high resolution in spectral characterization. So far, the reported Q factors of various THz sensors, in particular metamaterial and plasmonic ones, are very low because of the absorption and radiation loss.^[8, 11] Even by introducing the Fano resonance mechanism, metamaterial sensors made out of split-ring resonators generally have Q factors of less than 100.^[14] Recently, some of the authors have demonstrated a narrowband THz filter with a Q factor over 500 based on a grating waveguide (GW), where the low-loss guide-mode resonance (GMR) effect determines the filtering property.^[15] However, this GW with high-Q resonances is not advantageous for sensing because the electromagnetic fields are mostly confined within the waveguide with weak evanescent fields overlapped with the analyte outside.^[16, 17]

In this paper, we combine the unity-integrating configuration with the high-Q GMR resonance to push the THz sensing limit. It is realized by low-loss grating slot waveguides (GSWs), where liquid analytes flow in the slot layer and the incident THz wave is coupled into the slot waveguide by the gratings, resulting in a significant increase of the spatial overlap of the fields and the analyte. Both dielectric and metallic GSWs were investigated based on the coupled mode theory (CMT)^[18] and the finite difference time domain (FDTD) simulation. The advantages of GSW integrated microfluidic (GSWIM) sensors were presented by comparing with the GW and metamaterial sensors. The effects of the material and structure parameters on the sensing performance were investigated in detail, where an extremely high FoM of 692 was predicted as a result of simultaneous optimizations of the structural resonance and the spatial overlap between the sensing field and the analytes. Prototype devices were fabricated by assembling a silicon membrane and a quartz with gratings. The accuracy of the channel height and the divergence of the incident beam were discussed to explain the measured spectra. These sensors have a great potential application to detect real-time minor index changes or component changes in the analyzed substances.

2. Mechanism

For optical refractive index sensors, the amplitude variation (ΔI) and the resonant frequency shift (Δf) induced by the analytes index change (Δn) are usually used for monitoring the bio and chemo reactions (Section S1, Supporting information). A large frequency shift per unit of refractive index means a strong interaction between the optical field and the analyte indicating a sensitive device. For example, the higher-order modes of PC cavities can achieve a measured sensitivity S of 321 nm per RIU at a wavelength of 700nm.^[19] Plasmonic nanosphere/nanorod arrays can simulating realize a sensitivity of 500 nm per RIU ranging from UV to the near-infrared.^[20] A plasmonic perfect absorber based on U-shaped resonators was proposed with a sensitivity of 1445 nm per RIU in the infrared region.^[21] A metal-dielectric-metal waveguide sensor showed a sensitivity over 0.457 THz per RIU at 0.3-3 THz.^[22] In addition, the quality factor Q is another important parameter, which is defined as the ratio of f_0 to the full width at half maximum (FWHM). At a same S , the sensing system with a higher Q can be easier to detect the small signal. Therefore, a FoM is defined as the ratio of S to FWHM to consider all the factors.^[23, 24] So far, the highest FoM of 590 was achieved by using hyperbolic metamaterials with a sensitivity of 30000 nm per RIU at a wavelength of 1 μm .^[25] In the THz range, FoM is usually very small. For example, a calculated FoM of 5.2 had reported with a sensitivity of 14.5 μm per RIU based on the higher-order surface plasmon modes in a graphene strip.^[26] A PC cavity had realized a FoM of 19 with a Q factor over 10000 at 0.318 THz.^[27] A THz metamaterial consisting of periodic arrays of graphene rings with different radii had achieved a FoM of 17 with a sensitivity of 0.83 THz per RIU.^[24]

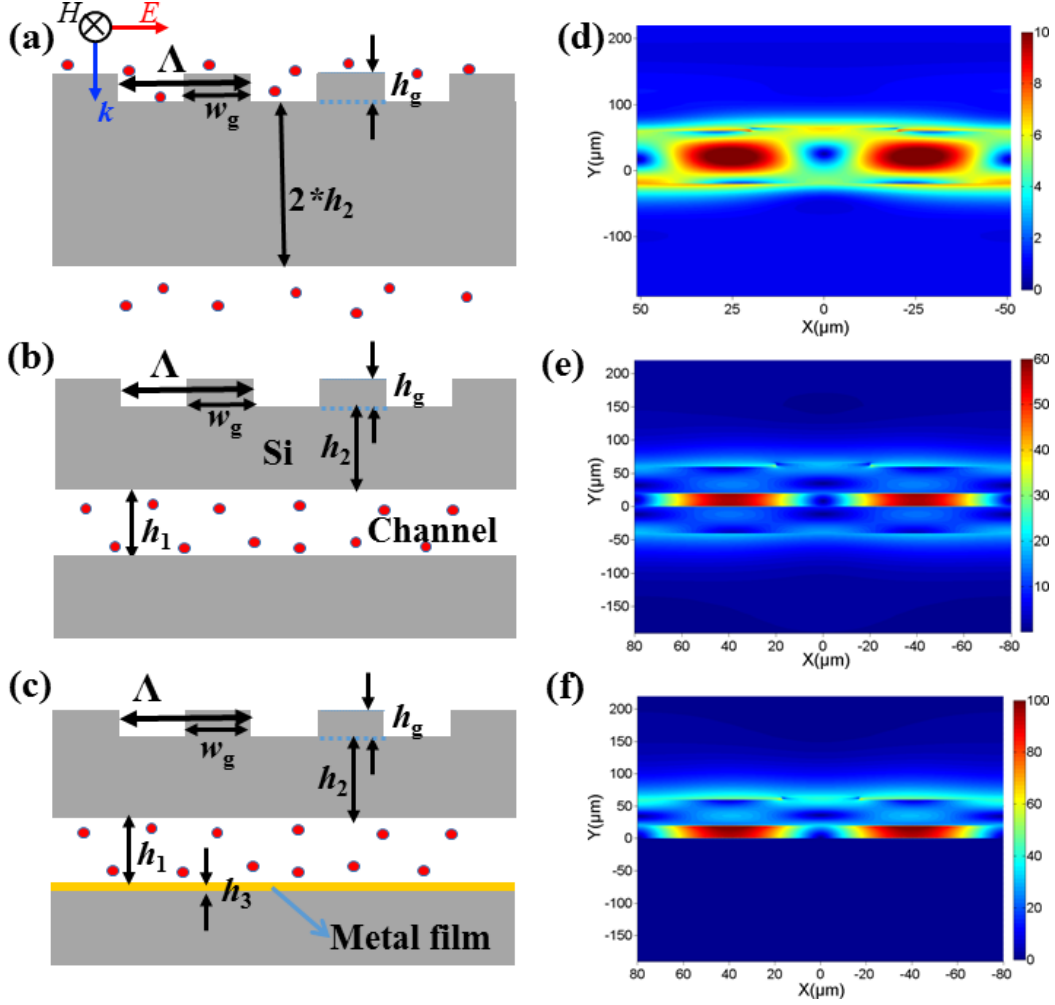


Figure 1 a) Schematic of the Si-GW. The period of the grating $\Lambda = 102 \mu\text{m}$, the height of the grating $h_g = 5 \mu\text{m}$, the width of grating $w_g = 40 \mu\text{m}$ and the height of the bulk silicon waveguide is $80 \mu\text{m}$. b) Schematic of the Si-GSW. $\Lambda = 160 \mu\text{m}$, $w_g = 40 \mu\text{m}$, $h_1 = 20 \mu\text{m}$, $h_2 = 40 \mu\text{m}$, and $h_g = 5 \mu\text{m}$. c) Schematic of the Al-GSW. $\Lambda = 160 \mu\text{m}$, $w_g = 34 \mu\text{m}$, $h_1 = 20 \mu\text{m}$, $h_2 = 40 \mu\text{m}$, $h_3 = 200\text{nm}$, and $h_g = 3 \mu\text{m}$. Electric field intensity distributions of the fundamental resonant mode in d) Si-GW, e) Si-GSW, and f) Si-GSW with a metal cladding are also shown. $n_{\text{si}} = 3.413 + i7.163 \times 10^{-5}$,^[28] $n_{\text{analyte}} = 1.5$, and the refractive index of Al is described by the Lorentz-Drude model.^[29]

Obviously, a sensing system with low radiation and absorption loss together with strong light-matter interaction is preferred. Compared to plasmonic and metamaterial,^[10, 14] the GMR effect (Section S2, Supporting Information) in a GW has a ultrahigh Q with a near-zero

absorption loss.^[30-32] As shown in Figure 1a, it is a typical GW where silicon gratings couple incident light into the guided mode in the lateral waveguide. Due to the low absorption loss of silicon and low radiation loss induced by the shallow gratings, Q is as high as 2466 at 0.977 THz, 176 times higher than that of the metamaterial perfect absorber.^[11] However, as shown in Figure 1d the resonant electromagnetic field is mostly confined in the waveguide with weak evanescent field overlapped with the analyte for sensing. Therefore, the sensitivity of this type of sensors is limited, for example, a sensitivity of 113 nm per RIU around 0.8 μ m was obtained in the GMR optical biosensors.^[31] Recently, some of the authors demonstrated a sensitive MA integrated microfluidic (MAIM) sensor, where the analyte channel was embedded into the MA at the position with the maximum electromagnetic field intensity.^[11] Driving by this idea, a GSW as shown in Figure 1b could provide much higher sensitivities and maintain high Q factors due to the greatly confined electromagnetic field inside the slot as shown in Figure 1e. The significantly increased overlap between the electromagnetic field and the analyte ensures a strong light-matter interaction. To quantitatively evaluate the sensitivity in a point of view of resonant field, we defined an intensity filling ratio (IFR), which is the ratio of the integral of the electric field intensity in the sensing region to that of the whole resonant fields. The calculated IFR is 23% in Figure 1d and 40% in Figure 1e. Therefore, although the analyte is assumed to enwrap the whole GW with a large volume, the light-matter interaction, that is, IFR, is still much less than that of the Si-GSW with a much smaller microfluidic channel volume. The above two free-standing structures are only used to discuss the physical mechanisms. For practical application, a Si-GSW with a metal cladding as shown in Figure 1c was proposed, where the metal film on a substrate is used to confine the resonant field instead of a silicon slab. The calculated Q and IFR are 5600 and 49% respectively indicating a promising performance.

3. Reflective GSWIM sensors

As discussed above, the metal-cladding GSW has a good potential for sensing. In this section, the performance is evaluated in details. As shown in Figure 2a, the gratings are on the upper surface of the Si membrane and the metallic reflector is on another silicon substrate with the inlet and outlet. The slot layer between the Si membrane and the metallic reflector functions as a microfluidic channel. By optimizing the silicon etching time, the height of the microfluidic channel and the gratings can be precisely controlled. The ultrathin cap is commercial products and also can be fabricated by general thinning techniques such as grinding, dry or wet etching.^[33, 34] When the incident THz beam shines on the silicon gratings, the on-resonance wave is coupled into the guided mode and interacts with the analyte. The reflected wave carrying the refractive index information of the analyte is detected and analyzed by the spectrometer. The reflection spectra were simulated with different analyte indices in the channel at the normal incidence *x*-polarized THz beams. As shown in Figure 2b, a high-Q single resonance with a local reflection minimum is observed in each case, where the FWHM of the resonant peak are 0.92, 0.74, 0.62, 0.56, 0.54, and 0.53GHz, respectively. The *Q*s (>1000) are much higher than the previous design based on metamaterial, fano resonance, plasmonics.^[10, 24, 35, 36] Moreover, the high *Q* factor is maintained at a wide range of refractive index n_1 from 1.3 to 1.8 covering most bio and chemo specimens. The near unity absorption of the incident THz wave is obtained at $n_1 = 1.5$, that is, all on-resonance incident THz beam is trapped and interacts with the analyte greatly enhancing the signal. The resonant frequency increases with the decreasing analyte index due to the decreasing effective resonant recycle as shown in Figure 2d. A fast analytical method was adopted to predict the upper and lower limits of the resonant frequency and the sensor sensitivity (Section S3, Supporting information). By treating the grating layer as an effective uniform layer, a slab structure with a silicon thickness of 40 or 45 μm , that is, the grating filling ratio (FR) of 0 or 1, provides two frequency limits of the actual GSW structure as shown by the two solid lines in Figure 2d. The

gradients of these two lines give an approximation of the sensitivity. In this case, the resonant peaks shift from 0.991 THz at $n_1=1.3$ to 0.873 THz at $n_1=1.8$, where the sensitivity is approximately 240 GHz per RIU. Accordingly, the resulted FoM is above 260 that is 44 times higher than the MAIM sensor. ^[11]

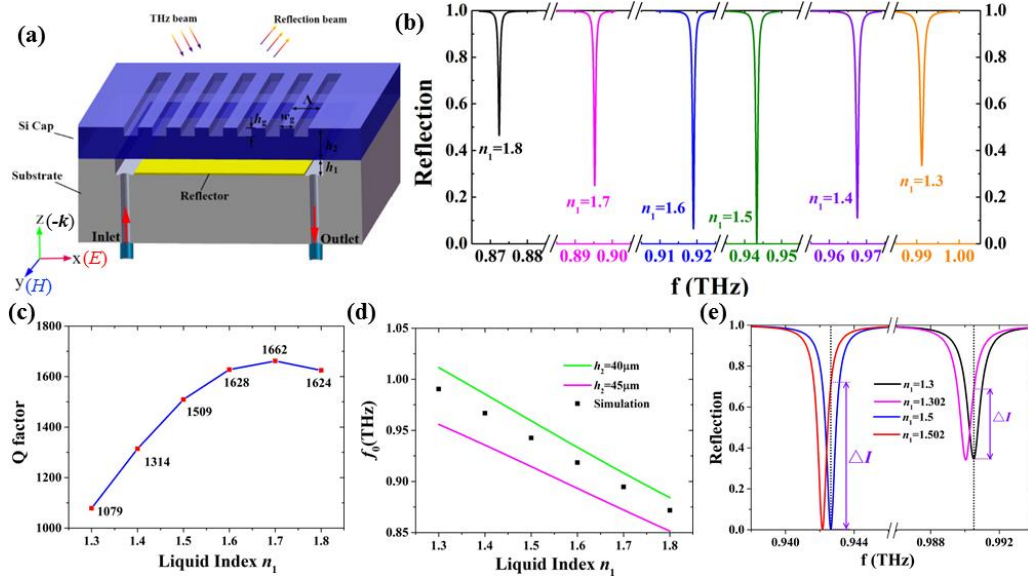


Figure 2 a) Schematic of the reflective metal-cladding GSWIM sensor. $\Lambda = 160 \mu\text{m}$, $w_g = 40 \mu\text{m}$, $h_1 = 20 \mu\text{m}$, $h_2 = 45 \mu\text{m}$, and $h_g = 5 \mu\text{m}$. b) Reflection spectra of the device for the analytes with different refractive indices. c) Q factors and d) f_0 versus the analyte indices. Black squares represent simulation results by the FDTD method. The magenta ($h_2 = 45 \mu\text{m}$) and green ($h_2 = 40 \mu\text{m}$) lines are results by the analytical method for two extreme cases, that is, FR=1 and 0. e) Reflection spectra of the sensor for detecting analytes with $\Delta n = 0.002$ around $n_1=1.3$ and 1.5.

Apart from the sensitivity defined by the frequency shift, the variation of intensity ΔI can also be used for signal detecting, ^[37] where the intensity sensitivity S_I is defined as the ratio of ΔI to Δn . In particular, when only single frequency source is available, this measurement is very useful. As seen from Figure 2b, the critical coupling condition is realized only at $n_1 = 1.5$, for example, more than 30% incidence was reflected at $n_1 = 1.3$. When the amplitude variation is used for sensing, the non-optimized coupling may degenerate the sensing performance.

Considering the small index variation $\Delta n = 0.002$ around $n_1 = 1.3$ and 1.5 , the associated spectra are shown in Figure 2e. The intensity sensitivity $S_I = 170$ per RIU and 350 per RIU respectively. It is preferable to have a constant high sensitivity in a broad detecting range. According to the CMT, the critical coupling condition for perfect absorption is $1/\tau_a = 1/\tau_r$ (Section S4, Supporting information), where $1/\tau_a$ is related to the propagation loss of TM mode and $1/\tau_r$ is related to the radiation loss by the gratings. Both $1/\tau_a$ and $1/\tau_r$ change with n_1 in a different way. As seen from Figure S3a, Supporting information, the deviation between $1/\tau_a$ and $1/\tau_r$ are nonnegligible in the case of reflective metal-cladding GSWIM, resulting in a distinct mismatch, that is, the non-zero reflection (Section S4, Supporting information). To address this issue, a metal-grating GSW structure as shown in Figure 3a is proposed, where the microfluidic channel is between a flat silicon membrane and metal-coated dielectric gratings. As seen from Figure S3b, Supporting information, the deviation between $1/\tau_a$ and $1/\tau_r$ in the case of a metal-grating GSW are much smaller than that of silicon-grating ones in a broad range of n_1 . Therefore, the critical coupling condition can be approximately matched. The reflection spectra of the metal-grating GSWIM sensor with different analyte indices are shown in Figure 3b. It can be seen that the minimum reflection at the resonant peaks for $n_1 = 1.1$ to 1.9 are all close to zero, that is, critical coupling maintains for all cases. Therefore, it is expected that this design provides better performance for most bio and chemo analytes. It is clear from Equation (S5), Supporting information, that no matter dielectric gratings or metal ones, the resonance occurs as long as the wave vector is matched. The physical mechanism in the metal grating structure is confirmed to be also GMR considering the relation between the resonance wavelengths and the period as shown in Figure S5a, Supporting information. In addition, the process of this structure design is easy because there is no need to fabricate micro-structures on the membrane. In simulation, the slope angle of the dielectric gratings was assumed to be

60° considering the imperfection of the fabrication. In fact, the slope angle was found to have little influence in the sensor performance.

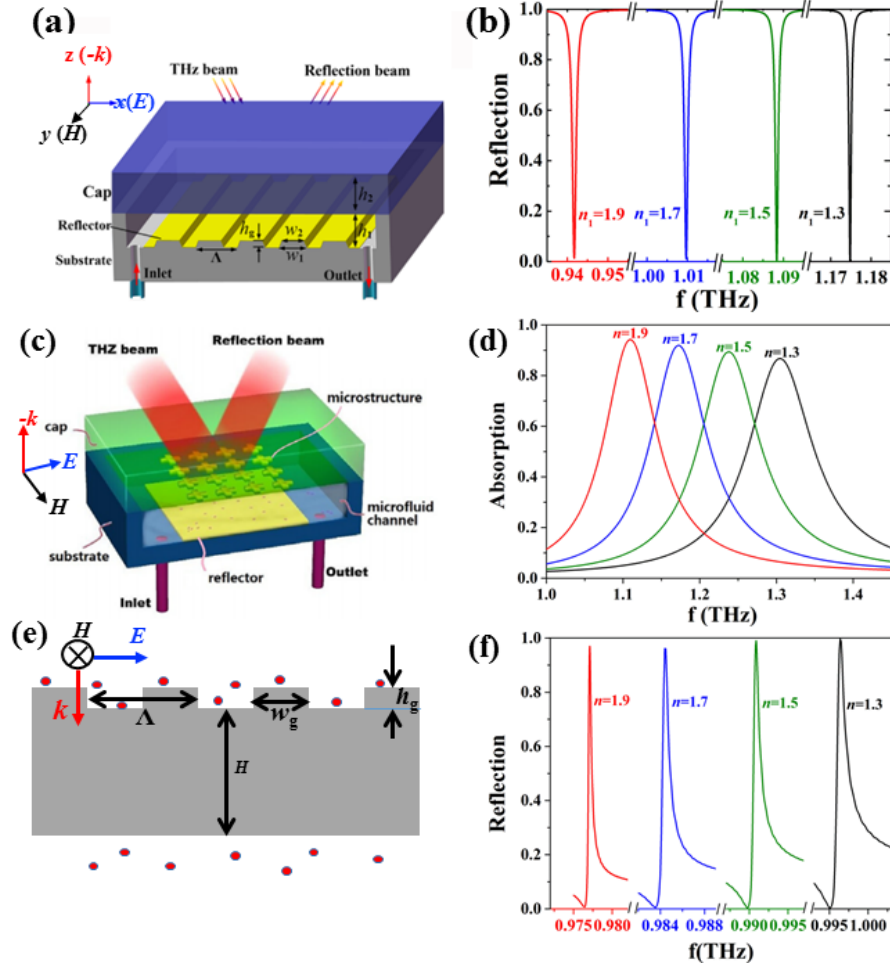


Figure 3 a) Schematic of the reflective metal-grating GSWIM sensor. b) Reflection spectra of GSWIM for the analytes with different refractive indexes. $\Lambda = 160 \mu\text{m}$, $w_1 = 75 \mu\text{m}$, $w_2 = 70.4 \mu\text{m}$, $h_1 = 30 \mu\text{m}$, $h_2 = 30 \mu\text{m}$, and $h_g = 4 \mu\text{m}$. c) Schematic of the MAIM sensor. d) Reflection spectra of MAIM for the analytes with different refractive indexes. The cap is semi-infinite quartz with the refractive index of 2.1. The reflector is chosen to be 200 nm gold with the refractive index is described by Drude mode. The period of microstructure is $52 \mu\text{m}$, the height of liquid channel is $5 \mu\text{m}$, the long and short side lengths of both arms of the metallic cross are 50 and $3 \mu\text{m}$, respectively. e) Schematic of the GWIM sensor. f) Reflection spectra of GWIM for the analytes with different refractive indexes. $\Lambda = 102 \mu\text{m}$, $h_g = 5 \mu\text{m}$, $w_g = 40 \mu\text{m}$ and $H = 80 \mu\text{m}$.

The MAIM sensor is known to have a large IFR of 66%^[11] due to the outstanding light trapping effect, which has been widely used in nanophotonic devices.^[38-40] The GWIM sensor is known to have a large Q over 570 at 785nm.^[41] To demonstrate the advantages of the unity-integrating of high Q and high IFR configurations in the proposed GSWIM sensors, these three types of sensors are compared as shown in Figure 3. As shown in the reflection spectra, the frequency shift with n_1 is large in the case of the MAIM sensor but with a very broad resonance peak. In contrast, the narrowband resonance is achieved in the GWIM sensor but with a very small frequency shift. Only in the case of GSWIM sensors, both the large frequency shift and the narrowband resonance are achieved. As shown in Figure S4, Supporting information, GSWIM and MAIM sensors usually have one-order of magnitude larger S than those of GWIM ones, meanwhile, GSWIM and GWIM sensors have two orders of magnitude higher Qs than those of MAIM ones. In details, the maximum sensitivity of 438 GHz per RIU is observed at $n_1 = 1.3$ with a Q of 1879 for the GSWIM sensor. The corresponding FoM reaches a record high value of 692. In contrast, the FoMs at $n_1 = 1.3$ for the MAIM and GWIM are only 4 and 18, respectively. In most cases, the proposed GSWIM sensor has a FoM of at least one order of magnitude higher than the other two types of sensors. The significantly improved performance of the proposed GSWIM sensor attributes to the unity-integrating configuration with simultaneous optimizations of the resonance mechanism and the spatial overlap between the sensing field and the analytes.

4. Transmissive GSWIM sensors

Although the reflective sensors have excellent performance, there are some limitations in the practical applications, for example, the oblique incidence is usually used instead of the normal incidence due to the spatial overlap of the illumination and collection light path. In addition, on-chip integration of the sensors to an imager or spectrometer prefers the transmissive version of the devices.^[42] As shown in Figure 4a, we propose a transmissive

GSWIM sensor, where the device configuration is similar to that in Figure 3a but the metallic gratings are on a flat substrate to allow the on-resonance transmission. Both the cap (high-resistance silicon membrane) and the substrate (high-density polyethylene, HDPE) are used to suppress the transmission loss of THz waves. In simulation, the refractive index of HDPE is assumed to be 1.6 ignoring the imaginary part and the gratings are made of aluminium. The transmission spectra with different analyte indices are shown in Figure 4b. There is a narrowband single transmission peak in a broad frequency region and the peak transmission of the device is as high as 80% with a very low background, which is ideal for transmissive sensing. From Figure 4c, we can see that most field intensity localized inside the channel with a large overlap with the analytes. There is a bright hot spot in the metal slit which might be used in the flow-through type nanophotonic sensors.^[43] The resonant frequency decreases linearly with the analyte index as shown in Figure 4d, from which the sensitivity is calculated to be 0.38 THz per RIU. The highest Q factor is over 2400 that is two orders of magnitude larger than metamaterial sensors.^[11] Besides, the associated FoM is above 180 that is 10 times higher than a terahertz metamaterial based on a dual-band graphene ring resonator.^[24] To demonstrate a potential application of the proposed THz GSWIM sensor, the transmission spectra for various Octane grades of gasoline were calculated and shown in Figure 4f. Distinct transmission peaks at different frequencies are easy to pick up from the spectra. The transmission changes 74% at 1.269 THz between gasoline #87 and #89, in contrast, it is less than 1% in the case of metallic nanohole array sensor.^[44] The effects of structural parameters of the transmissive GSWIM sensors were investigated in details in Section S6, Supporting information. Generally, a structure with a small index of the substrate and a small slit provides a distinct high Q transmission peak. Furthermore, the resonant frequency shows an obvious frequency shift with the incident angle.

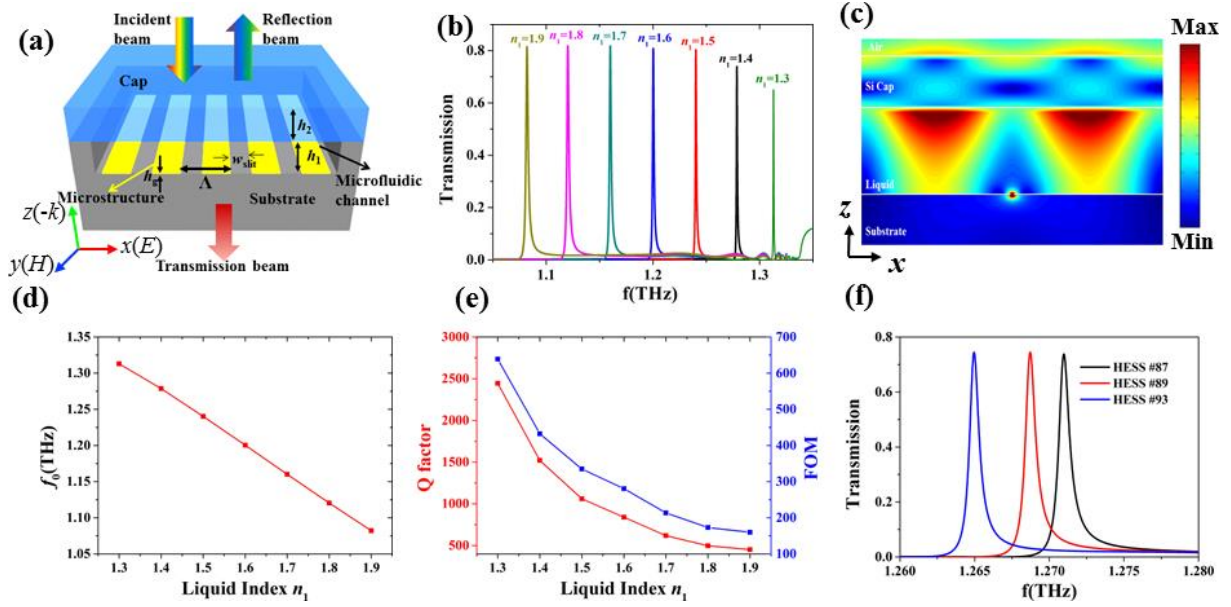


Figure 4 a) Schematic of a transmissive metal-grating GSWIM sensor. $\Lambda = 140\mu\text{m}$. $h_1 = 50\mu\text{m}$, $h_2 = 30\mu\text{m}$, $h_g = 0.2\mu\text{m}$ and $w_{\text{slit}} = 1\mu\text{m}$. b) Transmission spectra for the analytes with different refractive indices. c) Color maps of the electric field intensity at the resonance peak at $n_1 = 1.5$. d) The variation of resonance peak (f_0) for $n_1 = 1.3$ - 1.9 . e) The variation of Q factor and FoM for $n_1 = 1.3$ - 1.9 . f) The calculated transmission spectra of three different grades of gasoline with octane number of #87, #89, and #93. Refractive indices of various gasolines (#87, #89, and #93) are from Ref. [45].

5. Experiment and Discussion

Based on the design in the above sections, the transmissive GSWIM sensor was fabricated and the process flow is shown in Figure 5a. The packaged device as shown in Figure 5c consists of two components fabricated from two samples, that is, one is a quartz sample with metal microstructures and SU8 microfluidic channel, the other is a silicon-on-insulator (SOI) sample with a silicon membrane. The two parts were fabricated step-by-step as described in Figure 5a. The SOI sample has a silicon device layer of $20\mu\text{m}$, a SiO_2 buffer layer of $0.38\mu\text{m}$ and a silicon handling layer of $400\mu\text{m}$. The thickness of the SiO_2 layer and the aluminum layer is 200 and 200nm , respectively. For the cap sample, silicon membrane was obtained by the silicon and silicon oxide etch, which is surprisingly robust although it has a size of

10mm×10mm as shown by the square window in Figure 5c. The transmissive GSWIM sensor was achieved by assembling the cap and the substrate samples together using Teflon clamps as shown in Figure 5c. The channel height is determined by the thickness of spin-coated SU8 resist.

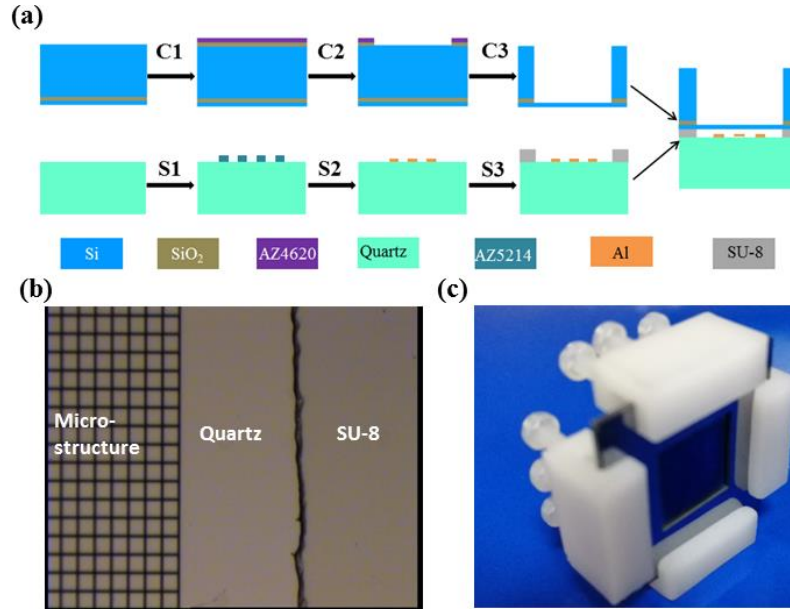


Figure 5 a) The process flow of the transmissive GSWIM sensor consisting of two parts. For the cap sample, a SiO₂ film is deposited on the back surface of the SOI sample followed by spin coating of a AZ4620 photoresist layer C1. Then, an opening is formed by photolithography and SiO₂ etch C2. Finally, the silicon handling layer and the silicon oxide layer of the SOI sample are etched through the opening C3. For the substrate sample, a AZ5214 photoresist layer is patterned into microstructure array. Then, aluminium microstructure array is formed by electron beam evaporation and liftoff. Finally, a microfluidic channel as a square seal is formed using the SU8 (Microchem) resist stripes by photolithography. b) The photograph of the quartz sample with aluminium microstructures and SU8 channel. c) The photograph of the packaged sample.

The schematic of the fabricated device is shown in Figure 6a. The structure parameters of the fabricated device are as follows: $\Lambda = 48 \mu\text{m}$, $h_2 = 20\mu\text{m}$, $h_1 = 4.32\mu\text{m}$, $w_{\text{slit}} = 5\mu\text{m}$, $h_g =$

200nm. The complex refractive index of the quartz substrate is assumed to be $2.17+0.0039i$. The calculated transmission spectra as a function of the channel height in Figure 6b. We can see three obvious transmission bands indicated by three arrows. With the increase of h_1 , all three bands show red shifts. These three bands look like broken around 2.8THz indicated by the white dash dot line, which is attributed to the Rayleigh anomaly.^[46] It is fixed for all the values of h_1 and only determined by the period of the metal structure and refractive index of substrate, that is, $\lambda=\Lambda(n_s \pm \sin\theta)$, where λ is the Rayleigh anomaly wavelength, n_s is the refractive index of substrate, θ is the incident angle. To find out the physical mechanism behind these three transmission bands, we calculate the transmission spectra of a similar structure to the one in Figure 6a but the metallic microstructure array is replaced by a flat metal film with a thickness of 10nm. For such a metal/dielectric multilayer structure, we also observe three transmission bands in Figure 6c at the similar places to those shown in Figure 6b, which are caused by the Fabry-Perot resonances in the metal/glucose/silicon cavity. Therefore, in the structure in Figure 6a, FP resonances still exist although the metal layer is patterned into microstructure array and they even dominate the transmission spectra especially for a large h_1 . For a small h_1 , for example $h_1=5\mu\text{m}$, we can see a local maximum and minimum around 2.4THz, which is the result of the coupling between the GMR and the FP resonance. As we notice, high Q GMR can be only observed in a range of h_1 , that is, $0.5\mu\text{m}$ to $10\mu\text{m}$. When h_1 is too small, the waveguide mode is cut off. When h_2 is too large, the coupling coefficient between the incident light and the well confined waveguide mode is too weak. Both cases cannot support a distinct transmission peak, which is a main reason for a missing high Q resonance in experiment. In Figure 6d, the measured transmission spectrum (Bruker IFS 66 v/s) of a device with glucose inside is shown together with a fitting spectrum $h_1=50\mu\text{m}$. There are three transmission peaks at 1.67THz, 2.35THz and 3.42THz indicated by three arrows in the measured spectrum, which agree well with the fitting spectrum. Therefore,

they are the FP resonances as marked by the three crossings of the black dot line and the three FP bands in Figure 6b. The peaks in the measured spectra were broaden because of the unevenness of the assembled substrate and the cap, which results in an average of the measured transmission at different h_1 . In addition, in the case of air in the microfluidic channel, the measured transmission spectrum in Figure 6e is also very similar to the simulation. The good match between the experiment and simulation confirms that our design and the simulation results are convincible. However, the narrowband transmission peak is not observed. As we can see, h_1 in the fitting spectra in Figure 6d,e are 50 and 38 μm respectively, which are much larger than what we expected in the optimized design. Because the high Q GMR can be only seen in a small range of h_1 as shown in Figure 6b,e, the large fabrication and assembling errors may be a main reason why we did not observe the high Q transmission peak. In the experiment, the cap sample has a flat top surface and the substrate sample has a square-ring shape SU8 resist seal on the top surface. When these two samples are packaged face to face, the channel is formed between the two surface and its height is determined by the thickness of SU8 resist. The missing of the GMR and the broadening of the FP resonances in the measured spectra are attributed to the error of h_1 in the actual experiment, which caused by the SU8 resist thickness error, the uneven assembling due to the uneven sample and the SU8 rim. Besides, current substrate quartz with a relatively high refractive index is not optimized as shown in Figure S5d, Supporting Information, where the high Q resonance becomes degenerate for the substrate refractive index over 2. Although these issues appear in current experiments, it could be solved in principle by optimizing the process and the used materials. For example, the microfluidic channel can be formed by dry etching the substrate accurately instead of using SU8 square ring, and the quartz substrate can be replaced by HDPE.

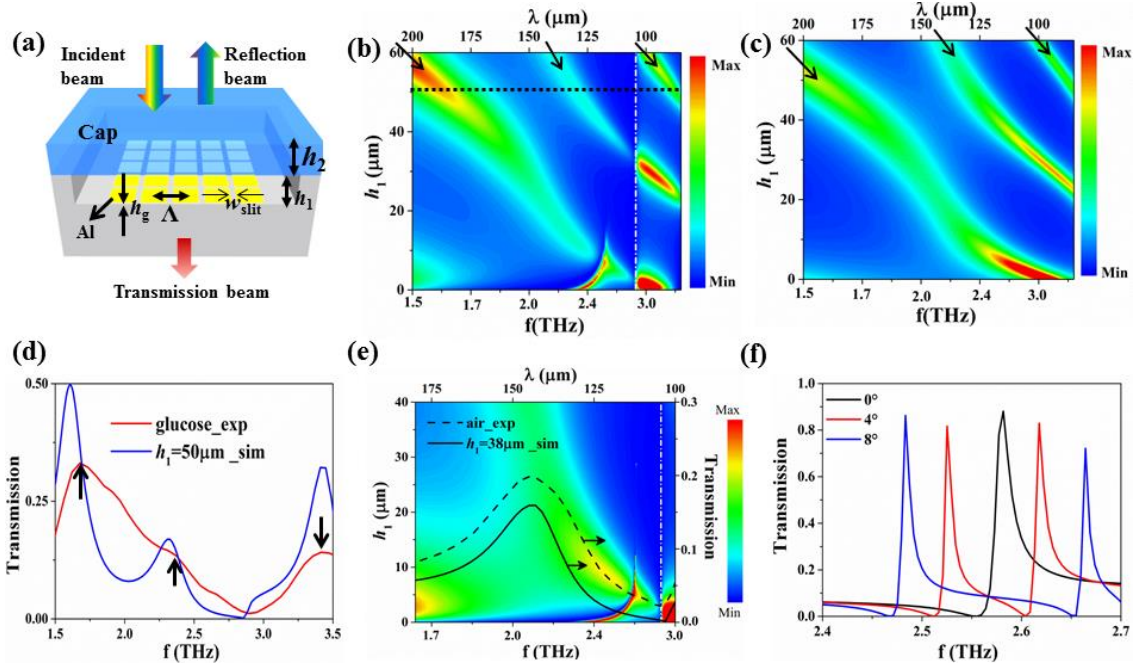


Figure 6 a) Schematic of the fabricated GSWIM sensor. b) The calculated transmission spectra versus the channel height h_1 in the case of glucose in the channel for a device as shown in (a). c) The calculated transmission spectra of a similar structure to the one in (a) but the metallic microstructure array is replaced by a flat metal film with a thickness of 10nm. d) The measured transmission spectrum of the device with glucose inside and the simulation result at $h_1=50\mu\text{m}$. e) The calculated transmission spectra versus the channel height h_1 in the case of air in the channel. In addition, the measured and its fitting spectra are shown in the black dashed and solid lines, respectively. f) The simulated spectra of the device with air in the channel at $h_1=2\mu\text{m}$ for the incident angle of 0° , 4° and 8° respectively. The silicon layer thickness of the cap is $h_2 = 21\mu\text{m}$. The refractive index of quartz and glucose is 2.17 and 1.7, respectively.

Apart from the error of h_1 , the divergence of the incident terahertz beam also has nonnegligible effect. As shown in Figure 6f, the transmission peak splits into two peaks and has obvious shifts for a small incident angle. A more than 50GHz shift of the resonant frequency was observed for a 4° oblique incidence. As a result, the measured spectra are actually the average of the transmission for a range of different incident angle, which may

broaden the peak and even kill the peak. The current spectral characterization is on a commercial THz-TDS system with a focused output beam. A more careful characterization need be done in future in a home-made TDS system with the customized lens-mirror group.

Finally, the calculated and experimental performances of various THz sensors in previous publications are summarized in Figure S8, Supporting information. As seen, the GSWIM devices support much higher Q factors than most other devices except the PC ones, and the sensitivities of the GSWIM devices are comparable to other devices except the MAIM ones. As a result, the GSWIM devices demonstrate a much higher calculated FoM. Although the experiments of the GSWIM sensors do not show the expected results so far due to the limitations in our experiments, the unity-integrating configuration with simultaneous optimizations of the resonance mechanism and the spatial overlap between the sensing field and the analytes is in principle able to deliver potential applications in monitoring molecular interactions and high-sensitivity matter detection. In addition, the proposed terahertz sensor is based on the detection of the resonance shift. Both the properties of high Q and high sensitivity are pursued to improve the detection technique of the resonance shift, which is similar to short wavelength sensing. As we know, a typical advantage of terahertz sensing is that many molecules have terahertz fingerprints which can be used for detection. Although we did not optimize our devices to a certain fingerprint wavelength, it could be easily done by adjusting the structure parameters as shown in Figure S5a, Supporting information, where the resonance frequency is tuned by changing the grating period. Once the high Q resonance with a large spatial overlap between the electromagnetic field and the analyte is achieved, the spectral fingerprint detection can be greatly improved. Furthermore, by making an array of high Q terahertz sensors at different frequencies, we can obtain the capability for multiple/parallel detection.

6. Conclusion

To summary, we proposed and experimentally demonstrated the unity integration of grating slot waveguide and microfluid for sensing, which is realized by incorporating the microfluidic channel as a slot layer into a GSW. As a result, both the amplitude and frequency sensitivities increase remarkably due to the greatly concentrated electromagnetic fields in the slot layer. Moreover, ultrahigh Q factors were achieved due to the low loss property of the GMR in the GSW. The calculated Q factors are two orders of magnitude larger than metamaterial sensors and the sensitivities are one order of magnitude larger than grating waveguide sensors. Extremely high FoM of 692 was predicted by numerical simulation. The devices were fabricated by assembling a silicon membrane and a quartz with metal gratings, showing reasonably good match between the experiment and calculation results considering the fabrication errors. The error of the microfluidic channel height and the divergence of the source beam degenerate the narrowband transmission peaks, which can be improved by optimization of fabrication process and measurement. The proposed unity-integrating configuration with simultaneous optimizations of the resonance mechanism and the spatial overlap between the sensing field and the analytes is a promising technique for high-sensitivity bio and chemo sensors.

Supporting Information

Supporting Information is available from the Wiley Online Library or from the author.

Acknowledgements

L.L. and X.H. contributed equally to this work. The authors are thankful for the technical support from Nano Fabrication Facility and Nano-X of SINANO, CAS. This work was supported by the grants from the National Natural Science Foundation of China (Nos. 61574158, 11774383, 11604367, and 21703083), the National Key Basic Research Program of China (No. 2014CB339806), the Royal Society Newton Advanced Fellowship, the Chinese Academy of Sciences President's International Fellowship Initiative (No. 2017DT0009), the

Cutting-edge Key Research Program of Chinese Academy of Sciences (No. QYZDBSSW-JSC014), Natural Science Foundation of Guangdong Province (Nos. 2017A030310463 and 2017A030313026).

Keywords

Guided-mode resonance, microfluidic, sensor, slot waveguide, terahertz

References

- [1] A. Menikh, R. MacColl, C. A. Mannella and X. C. Zhang, *Chem. Phys. Chem.* **2002**, 3,655.
- [2] M. Nagel, F. Richter, P. Haring-Bolívar and H. Kurz, *Phys. Med. Biol.* **2003**, 48, 3625.
- [3] X. Fan, I. M. White, S. I. Shopova, H. Zhu, J. D. Suter, Y. Sun, *Anal. Chim. Acta.* **2008**, 620, 8.
- [4] M. R. Lee, P. M. Fauchet, *Opt. Lett.* **2007**, 32, 3284.
- [5] A. Benz, C. Deutsch, M. Brandstetter, A. M. Andrews, P. Klang, H. Detz, W. Schrenk, G. Strasser, K. Unterrainer, *Sensors.* **2011**, 11, 6003.
- [6] M. Khorasaninejad, N. Abedzadeh, J. Walia, S. Patchett, S. S. Saini, *Nano Lett.* **2012**, 12, 4228.
- [7] A.G. Brolo, *Nat. Photonics.* **2012**, 6, 709.
- [8] G. Liu, M. He, Z. Tian, J. Li, J. Liu, *Appl. Opt.* **2013**, 52, 5695..
- [9] H. Tao, L. R. Chieffo, M. A. Brenckle, S. M. Siebert, M. Liu, A. C. Strikwerda, K. Fan, D. L. Kaplan, X. Zhang, R. D. Averitt, F. G. Omenetto, *Adv. Mater.* **2011**, 23, 3197.
- [10] R. Singh, W. Cao, I. Al-Naib, L. Cong, W. Withayachumnankul, W. Zhang, *Appl. Phys. Lett.* **2014**, 105, 171101.
- [11] X. Hu, G. Xu, L. Wen, H. Wang, Y. Zhao, Y. Zhang, D. R. S. Cumming, Q. Chen, *Laser Photonics Rev.* **2016**, 10, 962.

- [12] K. Bhattarai, Z. Ku, S. Silva, J. Jeon, J. O. Kim, S. J. Lee, A. Urbas, J. Zhou, *Adv. Opt. Mater.* **2015**, 3, 1779.
- [13] B. Ng, J. Wu, S. M. Hanham, A. I. Fern´andez-Dom´inguez, N. Klein, Y. F. Liew, M. B. H. Breese, M. Hong, S. A. Maier, *Adv. Opt. Mater.* **2013**, 1, 543.
- [14] L. Cong, M. Manjappa, N. Xu, I. Al-Naib, W. Zhang, R. Singh, *Adv. Opt. Mater.* **2015**, 3, 1537.
- [15] S. Song, F. Sun, Q. Chen, Y. Zhang, *IEEE Trans. Terahertz Sci. Technol.* **2015**, 5, 131.
- [16] G. Xiao, Q. Zhu, Y. Shen, K. Li, M. Liu, Q. Zhuang, C. Jin, *Nanoscale* **2015**, 7, 3429.
- [17] Y. Laamiri, F. Garet, J. L. Coutaz, *Appl. Phys. Lett.* **2009**, 94, 071106.
- [18] X. Hu, Q. Chen, L. Wen, L. Jin, H. Wang, W. Liu, *IEEE Photonics Technol. Lett.* **2016**, 28, 1665.
- [19] W. Liu, J. Yan, Y. Shi, *Opt. Express* **2017**, 25, 31739.
- [20] Y. C. Chau, C. Wang, L. Shen, C. M. Lim, H. Chiang, C. C. Chao, H. J. Huang, C. Lin, N. T. R. N. Kumara, N. Y. Voo, *Sci. Rep.* **2017**, 7, 16817.
- [21] Y. Cheng, X. S. Mao, C. Wu, L. Wu, R. Gong, *Opt. Mater.* **2016**, 53, 195.
- [22] X. Li, J. Song, J. X. J. Zhang, *Opt. Commun.* **2016**, 361, 130.
- [23] P. Offermans, M. C. Schaafsma, S. R. K. Rodriguez, Y. Zhang, M. Crego-Calama, S. H. Brongersma, J. G. Rivas, *ACS Nano* **2011**, 5, 5151.
- [24] C. Liu, P. Liu, C. Yang, L. Bian, *J. Opt.* **2017**, 19, 115102.
- [25] K. V. Sreekanth, Y. Alapan, M. ElKabbash, E. Ilker, M. Hinczewski, U. A. Gurkan, A. D. Luca, G. Strangi, *Nat. Mater.* **2016**, 15, 621.
- [26] O. V. Shapoval, A. I. Nosich, *J. Phys. D: Appl. Phys.* **2016**, 49, 055105.
- [27] K. Okamoto, K. Tsuruda, S. Diebold, S. Hisatake, M. Fujita, T. Nagatsuma, *J. Infrared Millim. Terahertz Waves* **2017**, 38, 1085.
- [28] Y. Laamiri, F. Garet, J. L. Coutaz, *Appl. Phys. Lett.* **2009**, 94, 071106.

- [29] A. D. Rakić, A. B. Djurić, J. M. Elazar, M. L. Majewski, *Appl. Opt.* **1998**, 37, 5271
- [30] B. Cunningham, B. Lin, J. Qiu, P. Li, J. Pepper, B. Hugh, *Sens. Actuator B-Chem.* **2002**, 85, 219.
- [31] Q. Wang, D. Zhang, H. Yang, C. Tao, Y. Huang, S. Zhuang, T. Mei, *Sensors* **2012**, 12, 9791.
- [32] S. M. Norton, G. M. Morris, T. Erdogan, *J. Opt. Soc. Am. A* **1998**, 15, 464.
- [33] A. W. Blakers, T. Armour, *Sol. Energy Mater. Sol. Cells* **2009**, 93, 1440.
- [34] S. Wang, B. D. Weil, Y. Li, K. X. Wang, E. Garnett, S. Fan, Y. Cui, *Nano Lett.* **2013**, 13, 4393.
- [35] Y. Z. Cheng, W. Withayachumnankul, A. Upadhyay, D. Headland, Y. Nie, R. Z. Gong, M. Bhaskaran, S. Sriram, D. Abbott, *Adv. Opt. Mater.* **2015**, 3, 376.
- [36] J. Wu, C. Zhang, L. Liang, B. Jin, I. Kawayama, H. Murakami, L. Kang, W. Xu, H. Wang, J. Chen, M. Tonouchi, P. Wu, *Appl. Phys. Lett.* **2014**, 105, 162602.
- [37] D. V. Nesterenko, S. Hayashi, Z. Sekkat, *Appl. Opt.* **2015**, 54, 4889.
- [38] L. Wen, Y. Chen, W. Liu, Q. Su, J. Grant, Z. Qi, Q. Wang, Q. Chen, *Laser Photonics Rev.* **2017**, 11, 1700059.
- [39] H. Wang, Q. Chen, L. Wen, S. Song, X. Hu, G. Xu, *Photonics Res.* **2015**, 3, 329.
- [40] L. Wen, F. Sun, Q. Chen, *Appl. Phys. Lett.* **2014**, 104, 151106.
- [41] R. Suresh, K. D. Rao, D. V. Udupa, S. Kumar, C. Prathap, N. K. Sahoo, *Optik* **2017**, 136, 112.
- [42] A. Shakoob, B. C. Cheah, D. Hao, M. Al-Rawhani, B. Nagy, J. Grant, C. Dale, N. Keegan, C. McNeil, D. R. S. Cumming, *ACS Photonics* **2016**, 3, 1926.
- [43] S. Aksu, A. A. Yanik, R. Adato, A. Artar, M. Huang, H. Altug, *Nano Lett.* **2010**, 10, 2511.

- [44] J. Li, Z. Tian, Y. Chen, W. Cao, Z. Zeng, *Appl. Opt.* **2012**, 51, 3258.
- [45] F. M. Al-Douser, Y. Chen, X. C. Zhang, *Int. J. Infrared Millim. Waves* **2007**, 27, 481.
- [46] M. S. Amin, J. W. Yoon, R. Magnusson, *Appl. Phys. Lett.* **2013**, 103, 131106